Published in IET Power Electronics
Received on 11th August 2010
Revised on 7th January 2011
doi: 10.1049/iet-pel.2010.0264

ISSN 1755-4535

Sensorless control of induction motors using multi-level converters

S. Kamel S. Mark A. Greg

Department of Electrical Engineering, Nottingham University, Nottingham, UK
E-mail: eezksks@exmail.nottingham.ac.uk

Abstract: This study describes a sensorless speed control scheme for induction motors supplied by a multi-level inverter. The scheme exploits the low DC link voltage used in some of the multi-level converter configurations which employ H-Bridges. The rotor position is tracked by measuring the rate of change of motor stator currents when low-voltage test vectors are applied using the H-Bridges. In this way, the motor current distortion introduced by the sensorless control scheme is reduced compared to that seen when using a two-level converter. The proposed approach could therefore be applied to high-power motor drives, and automotive drive systems. The study presents a theoretical derivation of the algorithm and experimental results which show the improvement in the motor current quality achieved using the new technique compared to sensorless techniques implemented on a two-level inverter.

1 Introduction

Sensorless control of induction motor drives using two-level inverters has been widely researched for systems employing standard two-level inverters. At low and zero speed, some form of additional excitation has been proposed, such as the injection of a high-frequency (HF) voltage or current [1–3] or the injection of test pulses [4–9]. However, these techniques introduce significant additional current distortion either because of the injected signals themselves (as in the HF injection methods and the INFORM method [4]) or owing to the insertion of the minimum pulse width in the operation of the drive system when applying the fundamental pulse width modulation (PWM) excitation method (FPE) [6]. This distortion causes audible noise, torque pulsations and increases the system losses.

The multi-level converter can achieve a higher voltage and power capability with conventional switching devices compared to two-level converters, and is now used for high-power drives [10]. It is also being proposed for specialist applications such as automotive drives [11]. Multi-level converters employ switching devices connected in a chain, which sequentially switch different DC voltages across the motor using a specialist PWM technique, to create a stepped output voltage. The particular structure of some of these converters offers significant potential for improving sensorless control of induction motors, as they employ H-Bridge circuits with a relatively low DC link voltage. For example, Lipo and co-workers [10] propose a multi-level topology which uses two cascaded H-Bridge circuits per phase. The first has a high DC link voltage, and employs gate turn-off thyristors (GTOs) or integrated gate commutated thyristors (IGCTs) as the switching devices which are controlled at relatively low frequency. The second uses a lower DC link voltage (e.g. 1/3 of the GTO DC link voltage) and employs IGBTs with a higher switching frequency. The combination of these circuits can provide a good quality voltage waveform for high-voltage applications. For sensorless control, the bridge with the lower DC link voltage can be used to reduce the current distortion introduced by both the two-level INFORM and FPE methods as it reduces the voltage distortion introduced by specific test pulses, and can also reduce the minimum duration of test pulses.

This paper describes the development of a sensorless control scheme for induction motors fed from a multi-level power converter. The paper first describes how the distortion is introduced into the motor current when the INFORM or FPE methods are employed, and then it outlines how the distortion is reduced by the multi-level approach. The author then go on to derive the sensorless control algorithm using multi-level converters. Results from a 16 kW experimental prototype are then presented to demonstrate excellent sensorless performance, and also the reduction in motor current distortion compared to the two-level INFORM and FPE methods.

2 Current distortion introduced using two-level converters

Both the INFORM and FPE sensorless control methods track the rotor slotting saliency in an induction motor by deriving an estimate of the drive's incremental inductance. This is achieved by measuring the motor current derivatives (di/dt) in response to specific voltage vectors applied to the motor. The INFORM [4] method applies these test vectors as specific pulses during the zero or null vectors of the normal PWM waveform. As these test vectors introduce a voltage

distortion, they create a change of current from the desired fundamental which must be compensated for. Therefore a further additional pulse is required to balance the original test pulse. The net results is a 'spike' appearing in the motor current waveform which increases the total harmonic distortion (THD) of the motor current, increases losses, audible noise and torque pulsations.

The FPE method [6] does not use specific test pulses. Instead it considers the normal voltage vectors employed by the fundamental PWM to be the test signals, and measures the motor current derivatives in response to these vectors. Ideally, there would be no additional distortion. Parasitic effects such as inter-turn capacitance in the motor, capacitance of the insulation between the IGBT and the heatsink, etc. result in HF current oscillations when the IGBTs switch states, and these take a few microseconds to die down [6]. The current derivatives required for the position estimation cannot be measured until these oscillations have disappeared. When the current derivative response to a particular switching vector must be measured, that vector must have a minimum duration t_{min}. Vectors shorter than t_{min} must be extended if position estimation is required during that switching period, and this results in significant distortion of the motor current. It should also be noted that the INFORM method requires a minimum pulse width for the same reason.

Fig. 1 illustrates the motor current distortion introduced using both the two-level INFORM and two-level FPE methods for sensorless control on the experimental system described later. In Fig. 1*a*, the INFORM method is used, and in this particular case vectors V1 and V4 are applied as test pulses during the zero vector V0 of the main fundamental PWM waveform [12] using a two-level inverter. The motor current is shown and the additional current ripple introduced by the test pulses has a peak value of around 3 A. Fig. 1*b* shows the current associated with the FPE method where the active vectors V1 and V2 are extended to (t_{min}) in the first half of the PWM period and are compensation by applying V4 and V5 in the second half of the PWM period to keep the volt time area unchanged. The extension and compensation introduce a peak current ripple of around 2 A.

Techniques have been proposed to reduce the 'spikes' associated with applying either the INFORM method and the FPE method. Robeischl and Schroedl [7] proposed an improved switching sequence for the INFORM method which employed additional inverter switching states to create a symmetric current deviation and to reduce the peak amplitude of the current ripple. The compromise with this approach is the addition of more switching events, increasing the switching losses in the drive Hua *et al.* [9] proposed a compensation method for the FPE method which adds additional switching vectors to the PWM period to reduce the distortion, but this then negates the advantages of the FPE method over the INFORM method.

The additional distortion in the current when applying the INFORM or FPE methods for sensorless control is a function of both the amplitude of the excitation voltage (test pulse or test vector) and minimum pulse width (t_{min}). This is the change of the voltage-time area caused by the change to the vector switching pattern over one switching period compared to that desired for control of the fundamental voltage only. To illustrate this, results for the INFORM method are shown from the experimental rig in Fig. 2. Fig. 2*a* shows the motor current response to a test pulse with an amplitude of 620 V (the typical DC link value for a conventional two-level inverter) and a reduced amplitude of 150 V using H-Bridges. The reduction of the peak of the current spike can clearly be seen. The disadvantage introduced by reducing the excitation voltage is that the signal-to-noise ratio (SNR) of the current derivative measurement will also be reduced, and therefore the SNR of the position estimate will deteriorate. Fig. 2*b* shows the reduction of the HF oscillations following a switching instant, if the excitation voltage is reduced from 620 to 150 V. The peak and duration of the oscillation are significantly reduced, allowing t_{min} to be changed from 25 to 20 μs. This also helps to reduce the peak current distortion.

3 Test pulses using the H-Bridge

A new scheme is introduced here to track the rotor position of an induction motor by tracking the rotor slotting saliency. The scheme can be considered as an 'INFORM'-type approach for multi-level converters which uses the measurement of current derivatives in response to test vectors imposed during the zero-switching vectors of a standard PWM scheme. In this

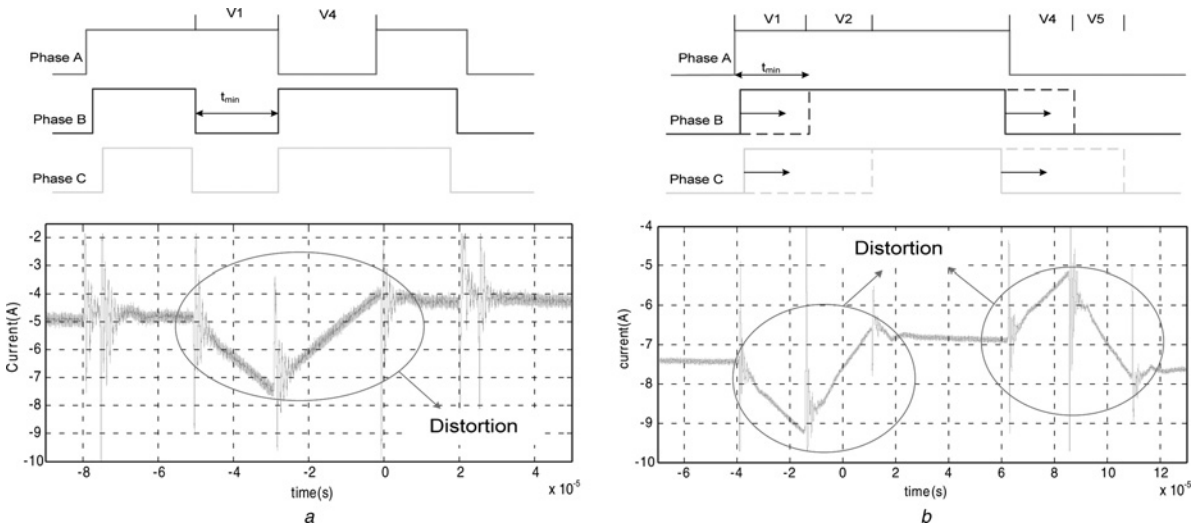

Fig. 1 *Motor current distortion using INFORM and FPE method*

a Dynamic current response in the two-level INFORM method
b Two-level fundamental PWM method

doi: 10.1049/iet-pel.2010.0264

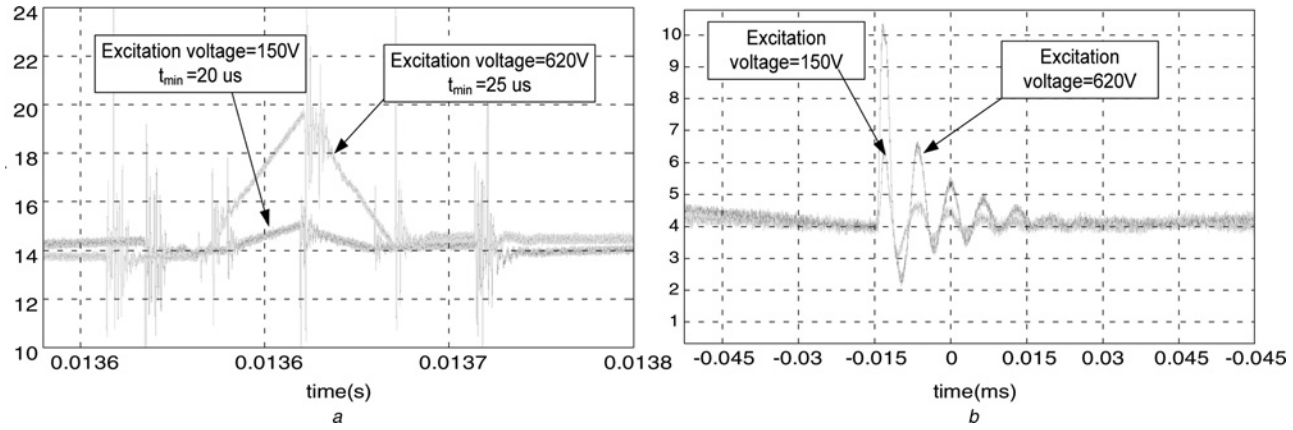

Fig. 2 *Reduction of HF oscillation*

a Effect of reducing the excitation voltage
b HF oscillation in the two-level INFORM method at different excitation voltages

case the test vectors are imposed using H-Bridge circuits connected in series with a main, two-level converter to generate test vectors with a voltage significantly smaller than the DC link voltage of the main inverter.

Fig. 3*a* shows the main circuit diagram for the prototype converter developed for this project. It consists of three H-Bridges connected in series with a standard inverter. This topology was chosen as it provides a relatively simple modification to a low-power two-level inverter, but can be used to verify the operation of the proposed algorithm. This topology has been proposed for specialist applications. For instance in [13], this topology is used to overcome the magnetic saturation problem in common mode chokes for passive compensation of common mode voltage in a PWM drive system. In [11], the same topology with a special modulation method is used to generate a five-level output voltage with only one power source used to supply both the standard inverter and the H-Bridges.

Fig. 3*b* shows the envisaged target topology proposed in [10], where three H-Bridges with a low DC link voltage and IGBT switches are connected in series with three H-Bridges consisting of IGCT switches and a higher DC link voltage. The topology of Fig. 3*a* can be used to verify sensorless control algorithms suitable for the topology of Fig. 3*b*, and is easier to develop as a low-power experimental prototype.

The multi-level INFORM method developed here uses current derivatives measured when test vectors are applied

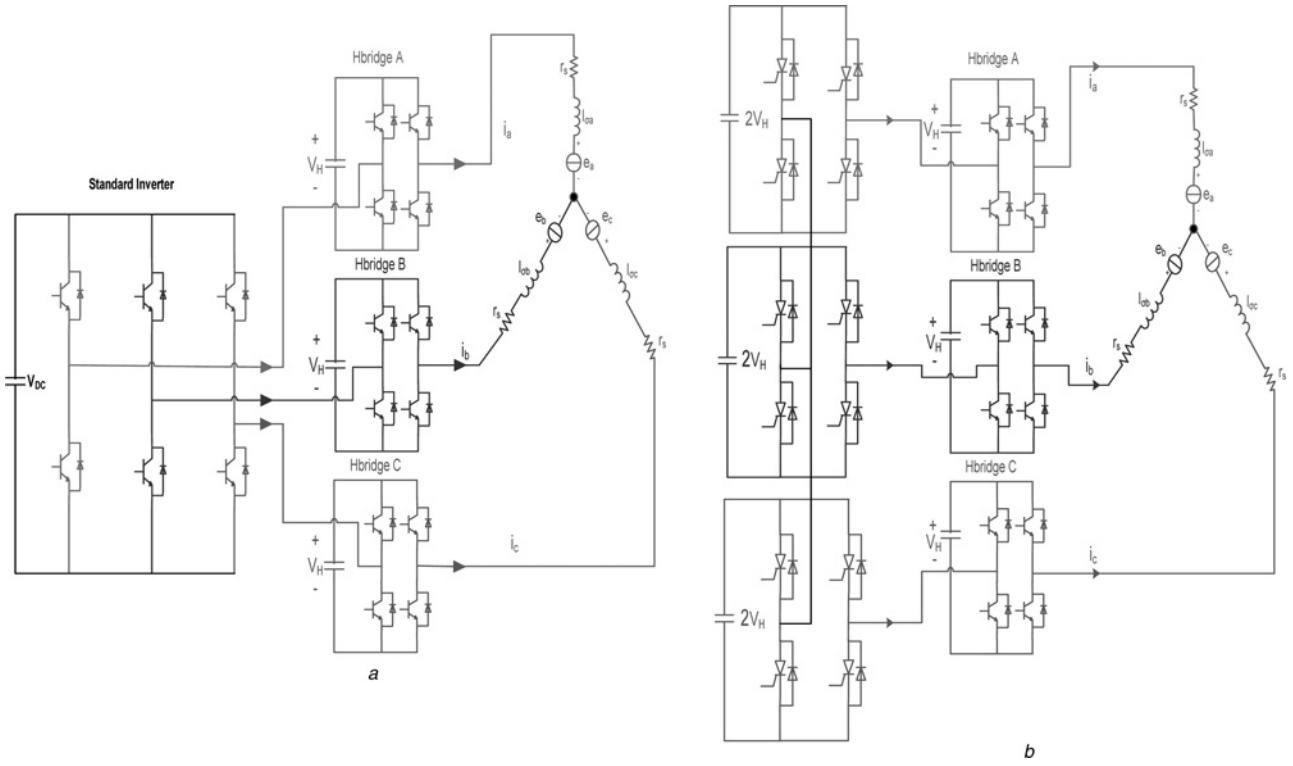

Fig. 3 *Envisaged target topology*

a Topology of the prototype multi-level converter
b Topology of the proposed high-power multi-level converter

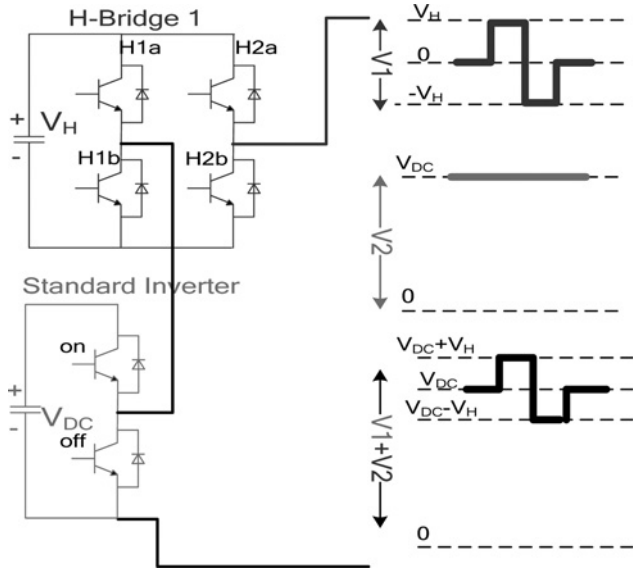

Fig. 4 *Output voltage waveform from the prototype topology*

using the lower H-Bridge voltage. For the proposed scheme, operation is considered, whereby the main motor voltage is derived using a standard space vector modulation with the two-level inverter. Test pulses are imposed using the H-Bridge during the zero-switching vectors of the main PWM waveform. Considering one phase of the system as shown in Fig. 4, the normal two-level PWM voltage is applied to the machine if IGBTs H1a and H2a are switched on, and H1b and H2b are switched off. A test pulse of $+V_H$ can be added to the phase voltage if IGBTs H1b and H2a are switched on, and similarly a test pulse of $-V_H$ can be added if IGBTs H1a and H2b are switched on, as shown in Fig. 4.

Fig. 5 shows the switching pattern that is generated using this topology to track the rotor slotting saliency. The figure also shows the sampling points for the current derivative measurements. During the application of the main inverter's null vector, one H-Bridge will be switched to generate positive and negative test pulses, whereas the other H-Bridges will generate a zero vector. This waveform is similar to that used in the two-level INFORM method [4] except in that a 150 V tests pulse is used instead of using 620 V test pulses. By applying the positive and negative test pulses together, (to keep the current distortion small) other advantages include being able to cancel the back emf effect in the sensorless algorithm (seen in the next section), and at the same time the voltage across the H-Bridges DC link can be easily maintained at a constant value.

4 Tracking the rotor slotting saliency

The rotor position is identified by tracking the rotor slotting saliency in the motor. The sensorless control algorithm is now described.

The stator leakage inductances of the induction motor are modulated by anisotropy – the effect considered here is the rotor slotting. The modulation can be expressed by the following equations

$$l_{\sigma a} = L_0 + \Delta L \cos(n_{an}\theta_{an}) \tag{1}$$

$$l_{\sigma b} = L_0 + \Delta L \cos\left(n_{an}\left(\theta_{an} - \frac{2\pi}{3}\right)\right) \tag{2}$$

$$l_{\sigma c} = L_0 + \Delta L \cos\left(n_{an}\left(\theta_{an} - \frac{4\pi}{3}\right)\right) \tag{3}$$

where L_0 is the average inductance and ΔL is the variation of leakage inductance owing to the rotor slotting (where $n_{an} = N_r/p$, N_r is the number of rotor slots and p is the number of pole pairs).

This modulation of the stator leakage inductances will be reflected in the transient response of the motor line current to the test vector imposed by the H-Bridges as shown in Fig. 2. By measuring the transient current response to the test vector it is possible to detect the inductance variation and track the rotor position and the algorithm required is derived in the following equations:

When H-Bridge A creates $+V_H$ test pulse during the zero vector of the main PWM waveform, the following equations can be derived using the machine equivalent circuit shown in Fig. 3

$$+V_H = \overbrace{r_s i_a + l_{\sigma a}\frac{di_a}{dt} + e_a - r_s i_b - l_{\sigma b}\frac{di_b}{dt} - e_b}^{(+V_H)} \tag{4}$$

$$0 = \overbrace{r_s i_b + l_{\sigma b}\frac{di_b}{dt} + e_b - r_s i_c - l_{\sigma c}\frac{di_c}{dt} - e_c}^{(+V_H)} \tag{5}$$

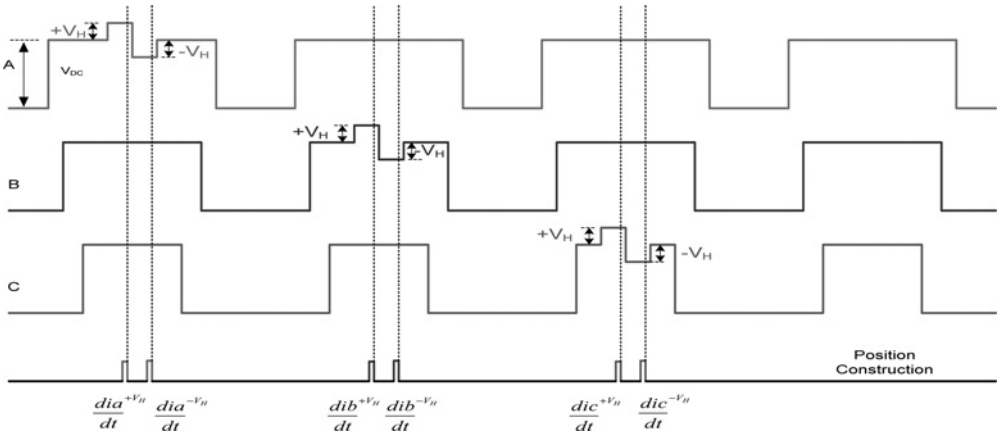

Fig. 5 *Switching pattern of the multi-level converter drive and the sequence for di/dt measurement and position construction*

doi: 10.1049/iet-pel.2010.0264

$$-V_{\mathrm{H}} = \overbrace{r_{\mathrm{s}} i_{\mathrm{c}} + l_{\sigma \mathrm{c}} \frac{\mathrm{d}i_{\mathrm{c}}}{\mathrm{d}t} + e_{\mathrm{c}} - r_{\mathrm{s}} i_{\mathrm{a}} - l_{\sigma \mathrm{a}} \frac{\mathrm{d}i_{\mathrm{a}}}{\mathrm{d}t} - e_{\mathrm{a}}}^{(+V_{\mathrm{H}})} \quad (6)$$

where $+V_{\mathrm{H}}$ is the H-Bridge DC Link voltage, r_{s} is the stator resistance per phase and e_{a} is the back emf in phase a.
The superscripts $\overbrace{\ }^{(+V_{\mathrm{H}})}$ denote that the measurement is made during the $+V_{\mathrm{H}}$ test pulse.

In a similar way, when H-Bridge A generates the $-V_{\mathrm{H}}$ test pulse the following equations can be derived

$$-V_{\mathrm{H}} = \overbrace{r_{\mathrm{s}} i_{\mathrm{a}} + l_{\sigma \mathrm{a}} \frac{\mathrm{d}i_{\mathrm{a}}}{\mathrm{d}t} + e_{\mathrm{a}} - r_{\mathrm{s}} i_{\mathrm{b}} - l_{\sigma \mathrm{b}} \frac{\mathrm{d}i_{\mathrm{b}}}{\mathrm{d}t} - e_{\mathrm{b}}}^{(-V_{\mathrm{H}})} \quad (7)$$

$$0 = \overbrace{r_{\mathrm{s}} i_{\mathrm{b}} + l_{\sigma \mathrm{b}} \frac{\mathrm{d}i_{\mathrm{b}}}{\mathrm{d}t} + e_{\mathrm{b}} - r_{\mathrm{s}} i_{\mathrm{c}} - l_{\sigma \mathrm{c}} \frac{\mathrm{d}i_{\mathrm{c}}}{\mathrm{d}t} - e_{\mathrm{c}}}^{(-V_{\mathrm{H}})} \quad (8)$$

$$+V_{\mathrm{H}} = \overbrace{r_{\mathrm{s}} i_{\mathrm{c}} + l_{\sigma \mathrm{c}} \frac{\mathrm{d}i_{\mathrm{c}}}{\mathrm{d}t} + e_{\mathrm{c}} - r_{\mathrm{s}} i_{\mathrm{a}} - l_{\sigma \mathrm{a}} \frac{\mathrm{d}i_{\mathrm{a}}}{\mathrm{d}t} - e_{\mathrm{a}}}^{(-V_{\mathrm{H}})} \quad (9)$$

Since the time between applying the $+V_{\mathrm{H}}$ and $-V_{\mathrm{H}}$ test vectors is very short, it can be assumed that

$$\overbrace{e_{\mathrm{a}}}^{(+V_{\mathrm{H}})} = \overbrace{e_{\mathrm{a}}}^{(-V_{\mathrm{H}})}, \ \overbrace{e_{\mathrm{b}}}^{(+V_{\mathrm{H}})} = \overbrace{e_{\mathrm{b}}}^{(-V_{\mathrm{H}})}, \ \overbrace{e_{\mathrm{c}}}^{(+V_{\mathrm{H}})} = \overbrace{e_{\mathrm{c}}}^{(-V_{\mathrm{H}})}$$

Also as the voltage across the stator resistance is small compared to the H-Bridge voltages $+V_{\mathrm{H}}$ and $-V_{\mathrm{H}}$, it can be neglected.

Subtracting (7)–(9) from (4)–(6), respectively, the following equations are obtained

$$+2V_{\mathrm{H}} = l_{\sigma \mathrm{a}} \left(\overbrace{\frac{\mathrm{d}i_{\mathrm{a}}}{\mathrm{d}t}}^{(+V_{\mathrm{H}})} - \overbrace{\frac{\mathrm{d}i_{\mathrm{a}}}{\mathrm{d}t}}^{(-V_{\mathrm{H}})} \right) - l_{\sigma \mathrm{b}} \left(\overbrace{\frac{\mathrm{d}i_{\mathrm{b}}}{\mathrm{d}t}}^{(+V_{\mathrm{H}})} - \overbrace{\frac{\mathrm{d}i_{\mathrm{b}}}{\mathrm{d}t}}^{(-V_{\mathrm{H}})} \right) \quad (10)$$

$$0 = l_{\sigma \mathrm{b}} \left(\overbrace{\frac{\mathrm{d}i_{\mathrm{b}}}{\mathrm{d}t}}^{(+V_{\mathrm{H}})} - \overbrace{\frac{\mathrm{d}i_{\mathrm{b}}}{\mathrm{d}t}}^{(-V_{\mathrm{H}})} \right) - l_{\sigma \mathrm{c}} \left(\overbrace{\frac{\mathrm{d}i_{\mathrm{c}}}{\mathrm{d}t}}^{(+V_{\mathrm{H}})} - \overbrace{\frac{\mathrm{d}i_{\mathrm{c}}}{\mathrm{d}t}}^{(-V_{\mathrm{H}})} \right) \quad (11)$$

$$-2V_{\mathrm{H}} = l_{\sigma \mathrm{c}} \left(\overbrace{\frac{\mathrm{d}i_{\mathrm{c}}}{\mathrm{d}t}}^{(+V_{\mathrm{H}})} - \overbrace{\frac{\mathrm{d}i_{\mathrm{c}}}{\mathrm{d}t}}^{(-V_{\mathrm{H}})} \right) - l_{\sigma \mathrm{a}} \left(\overbrace{\frac{\mathrm{d}i_{\mathrm{a}}}{\mathrm{d}t}}^{(+V_{\mathrm{H}})} - \overbrace{\frac{\mathrm{d}i_{\mathrm{a}}}{\mathrm{d}t}}^{(-V_{\mathrm{H}})} \right) \quad (12)$$

From (10) and (12) it is possible to derive

$$\left(\overbrace{\frac{\mathrm{d}i_{\mathrm{a}}}{\mathrm{d}t}}^{(+V_{\mathrm{H}})} - \overbrace{\frac{\mathrm{d}i_{\mathrm{a}}}{\mathrm{d}t}}^{(-V_{\mathrm{H}})} \right) = \frac{+2V_{\mathrm{H}}(l_{\sigma \mathrm{b}} + l_{\sigma \mathrm{c}})}{(l_{\sigma \mathrm{a}} l_{\sigma \mathrm{b}} + l_{\sigma \mathrm{b}} l_{\sigma \mathrm{c}} + l_{\sigma \mathrm{c}} l_{\sigma \mathrm{a}})} \quad (13)$$

Using (1)–(3) the quantity $l_{\sigma \mathrm{a}} l_{\sigma \mathrm{b}} + l_{\sigma \mathrm{b}} l_{\sigma \mathrm{c}} + l_{\sigma \mathrm{c}} l_{\sigma \mathrm{a}}$ can be substituted by $3L_0(1 - (\Delta L/2L_0)^2)$ and hence (13) can be rewritten as

$$\left(\overbrace{\frac{\mathrm{d}i_{\mathrm{a}}}{\mathrm{d}t}}^{(+V_{\mathrm{H}})} - \overbrace{\frac{\mathrm{d}i_{\mathrm{a}}}{\mathrm{d}t}}^{(-V_{\mathrm{H}})} \right) = \frac{-2V_{\mathrm{H}}(2L_0 - \Delta L \cos(n_{\mathrm{an}} \theta_{\mathrm{an}}))}{3L_0 \left(1 - \left(\Delta L/2L_0\right)^2\right)} \quad (14)$$

By defining the constant

$$g = \frac{3\left(1 - \left(\Delta L/2L_0\right)^2\right)}{2v_{\mathrm{H}}}$$

Equation (14) can be rewritten as follows

$$\left(\overbrace{\frac{\mathrm{d}i_{\mathrm{a}}}{\mathrm{d}t}}^{(+V_{\mathrm{H}})} - \overbrace{\frac{\mathrm{d}i_{\mathrm{a}}}{\mathrm{d}t}}^{(-V_{\mathrm{H}})} \right) = \frac{-2}{g} + \frac{\Delta L \cos(n_{\mathrm{an}} \theta_{\mathrm{an}})}{g * L_0}$$

or (15)

$$\frac{\Delta L \cos(n_{\mathrm{an}} \theta_{\mathrm{an}})}{L_0} = 2 + g \left(\overbrace{\frac{\mathrm{d}i_{\mathrm{a}}}{\mathrm{d}t}}^{(+V_{\mathrm{H}})} - \overbrace{\frac{\mathrm{d}i_{\mathrm{a}}}{\mathrm{d}t}}^{(-V_{\mathrm{H}})} \right)$$

Also (1) can be rewritten as

$$\frac{l_{\sigma_{\mathrm{a}}}}{L_0} - 1 = \frac{\Delta L \cos}{L_0} (n_{\mathrm{an}} \theta_{\mathrm{an}}) \quad (16)$$

Substituting (16) in (15) yields

$$\frac{l_{\sigma_{\mathrm{a}}}}{L_0} = 3 + g \left(\overbrace{\frac{\mathrm{d}i_{\mathrm{a}}}{\mathrm{d}t}}^{(+V_{\mathrm{H}})} - \overbrace{\frac{\mathrm{d}i_{\mathrm{a}}}{\mathrm{d}t}}^{(-V_{\mathrm{H}})} \right) \quad (17)$$

Which means that the inductance in phase a can be measured by measuring the quantity $\left(\overbrace{\mathrm{d}i_{\mathrm{a}}/\mathrm{d}t}^{(+V_{\mathrm{H}})} - \overbrace{\mathrm{d}i_{\mathrm{a}}/\mathrm{d}t}^{(-V_{\mathrm{H}})} \right)$. The rotor slotting position scalar for the a phase can then be defined as

$$P_{\mathrm{a}} = 2 + \mathrm{g} \left(\overbrace{\frac{\mathrm{d}i_{\mathrm{a}}}{\mathrm{d}t}}^{(+V_{\mathrm{H}})} - \overbrace{\frac{\mathrm{d}i_{\mathrm{a}}}{\mathrm{d}t}}^{(-V_{\mathrm{H}})} \right) \quad (18)$$

Repeating for phases b and c yields the following equations for slotting position scalars P_{b}, P_{c}

$$P_{\mathrm{b}} = 2 + \mathrm{g} \left(\overbrace{\frac{\mathrm{d}i_{\mathrm{b}}}{\mathrm{d}t}}^{(+V_{\mathrm{H}})} - \overbrace{\frac{\mathrm{d}i_{\mathrm{b}}}{\mathrm{d}t}}^{(-V_{\mathrm{H}})} \right) \quad (19)$$

$$P_{\mathrm{c}} = 2 + \mathrm{g} \left(\overbrace{\frac{\mathrm{d}i_{\mathrm{c}}}{\mathrm{d}t}}^{(+V_{\mathrm{H}})} - \overbrace{\frac{\mathrm{d}i_{\mathrm{c}}}{\mathrm{d}t}}^{(-V_{\mathrm{H}})} \right) \quad (20)$$

The final form for the alpha and beta components of the rotor slot position scalar will be

$$P_\alpha = P_a - \frac{1}{2}(P_b + P_c) \tag{21}$$

$$P_\beta = \frac{\sqrt{3}}{2}(P_b + P_c) \tag{22}$$

The scalar position signals, P_α and P_β are similar to resolver signals, and the rotor position can be extracted from them using further signal processing.

5 Estimated rotor position and disturbance filtering

The anisotropy caused by the rotor slotting using the proposed method is tracked by measuring di/dt in response to test vectors. The position signals $P\alpha$ and $P\beta$ for an induction motor with 28 rotor slots operating at 15 rpm and 50% load are shown in Fig. 6. (The experimental system is described in the next section.)

As well as the rotor slotting saliency ($14f_r$), other disturbance harmonics are observed in Fig. 6, which make the position signals difficult to use. The ($2f_e$) and (f_e) components are owing to the saturation in the machine and the unbalance in the di/dt sensors, respectively, and the component ($14f_r + 2f_e$) arises because the position signal ($14f_r$) is also modulated by the saturation in the machine ($2f_e$) [5].

To remove the ($2f_e$) and (f_e) components, a synchronous filter based on the low-memory disturbance elemination method [14] is used which assumes that the phase and amplitude of these disturbance harmonics will only change as a function of load, and is independent of speed. These disturbance harmonics can be calibrated for different loads using a commissioning process [14] and stored in memory. They are then used online for compensating the raw position signal, and are extracted from the look-up table as a function of the torque producing current i_q as shown for the $2f_e$ component in Fig. 7*a*.

The filtering of the disturbace ($14f_r + 2f_e$) is achieved by using a synchronous filter in the rotating frame $14\theta_r + 2\theta_e$ [15] as shown in Fig. 7*b*. The low-pass filter has a cut-off frequency of 0.5 Hz.

The position signals after both the synchronous and sideband filters are shown in Fig. 8. It can be seen that the rotor slotting effect is now much stronger and is now suitable for rotor position tracking.

6 Experimental results

The proposed method has been implemented on an indirect rotor field orientation controlled squirrel cage, star connected, four pole, 16 kW, 50 Hz induction motor with 28 semi-closed rotor slots. The switching frequency of the main inverter was 5 kHz, and the DC link voltage used for the H-Bridges was 150 V. The width of the H-Bridge test vectors was 20 μs. The rated current for the H-Bridges was 70% of the machine-rated load. Therefore testing was restricted to 50% of the rated load of the machine.

The filtered α and β components of the position signal are used with a mechanical observer as described in [16] to derive the rotor speed from the slotting frequency, and to enhance the quality of the estimated speed and position. The estimated rotor position and speed are then used for field orientation and speed feedback in a sensorless speed control system as shown in Fig. 9. The speed control was designed to have a bandwidth of 6 rad/s.

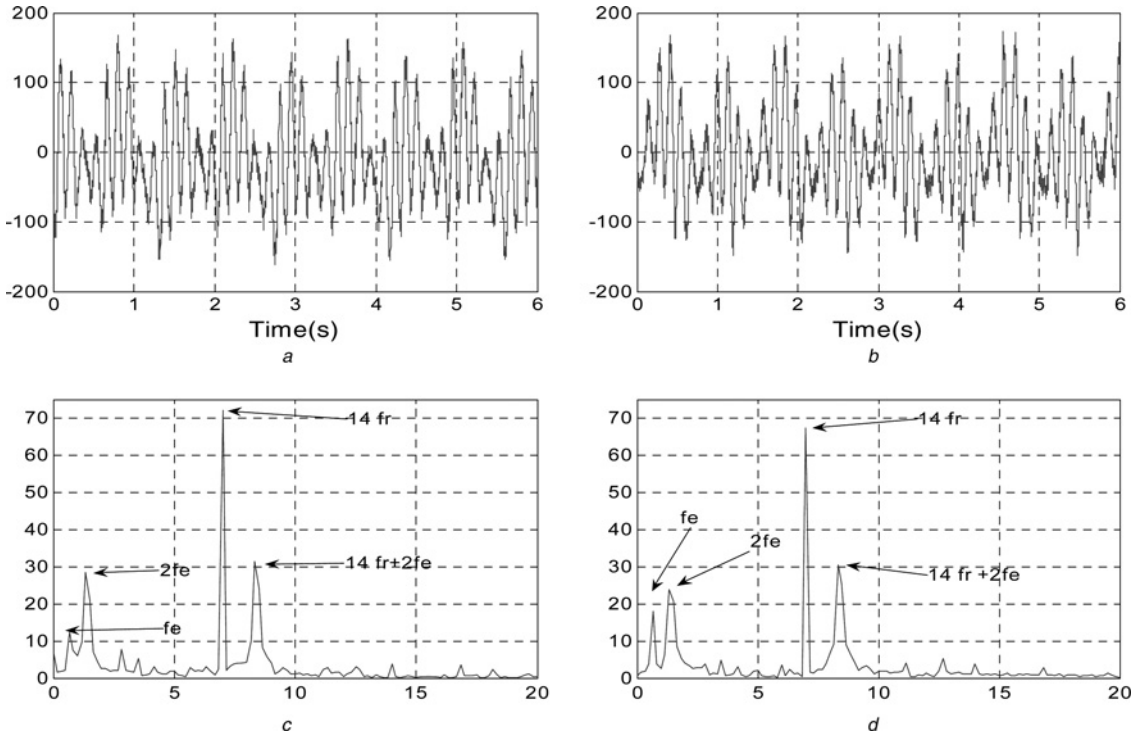

Fig. 6 *Position signals Pα and Pβ for an induction motor with 28 rotor slots operating at 15 rpm and 50%*

a and *b* α and β components of the estimated position signal at 15 rpm, 50% load
c and *d* Frequency spectrum of α and β components of the estimated position signal

doi: 10.1049/iet-pel.2010.0264

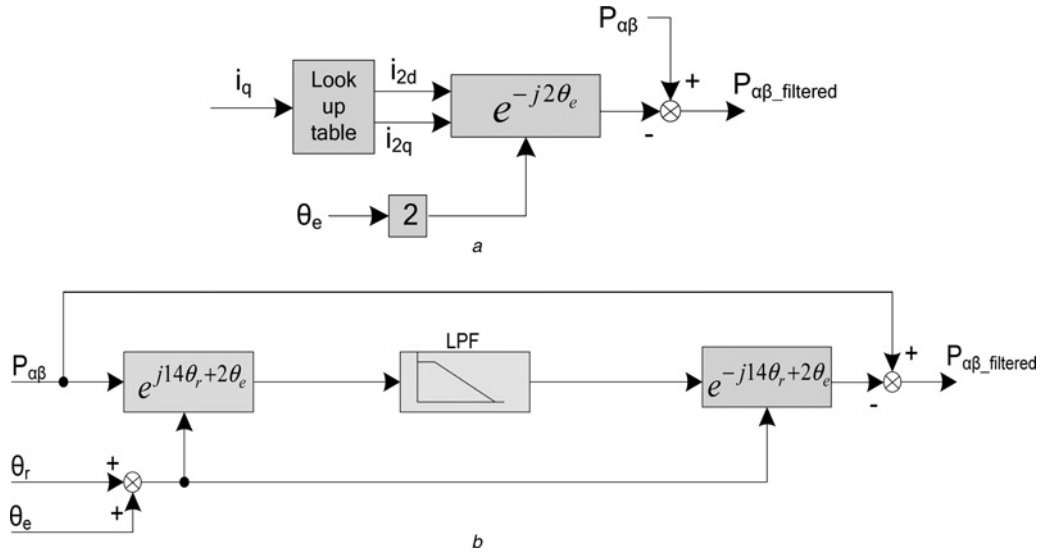

Fig. 7 *Disturbance harmonics calibrated for different loads using a commissioning process and stored in memory*

a Schematic of the memory-based synchronous filter
b Schematic of the side band filter

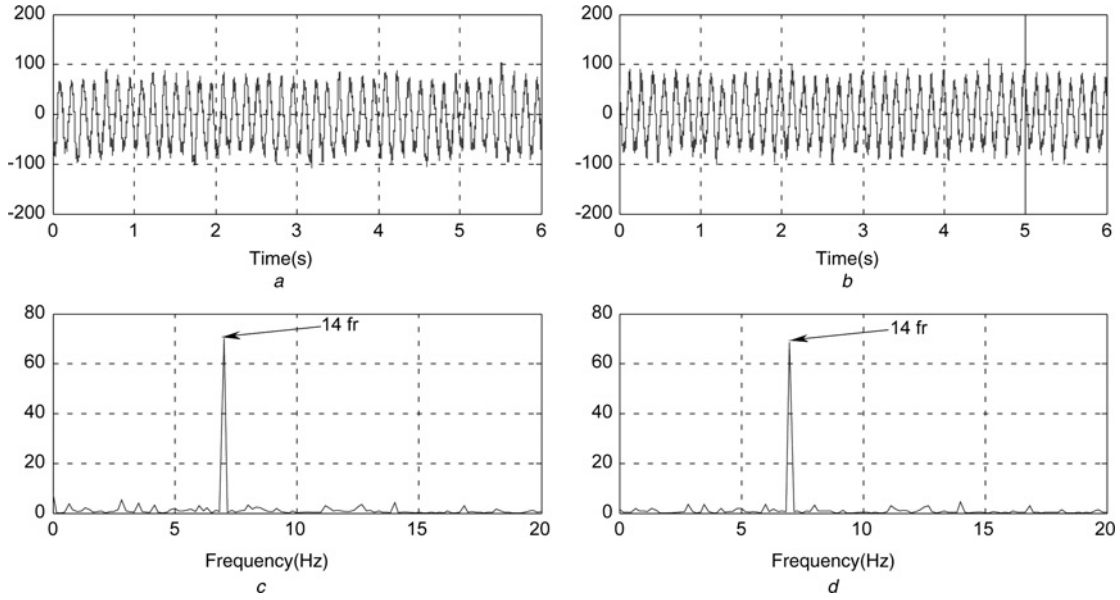

Fig. 8 *Estimated rotor position and disturbance filtering*

a and *b* Filtered α and β component of the estimated position at 15 rpm, 50% load
c and *d* FFT of α and β component of the estimated position

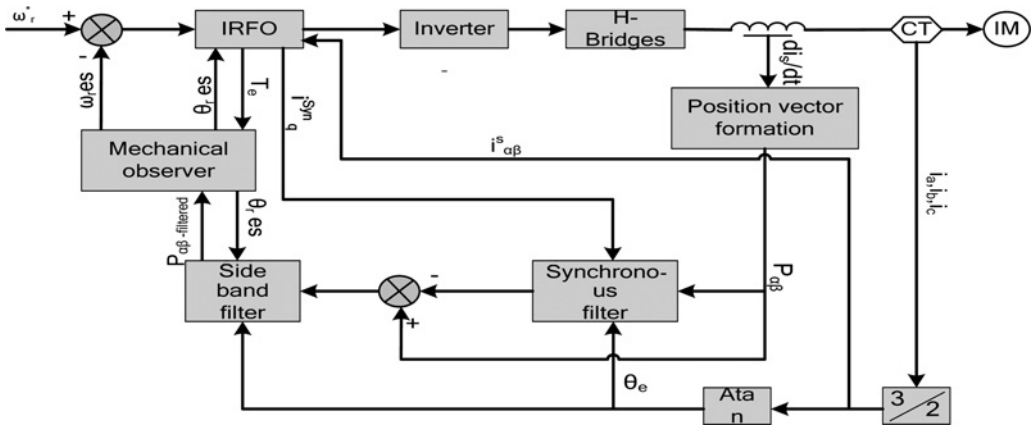

Fig. 9 *System set-up of the sensorless speed control*

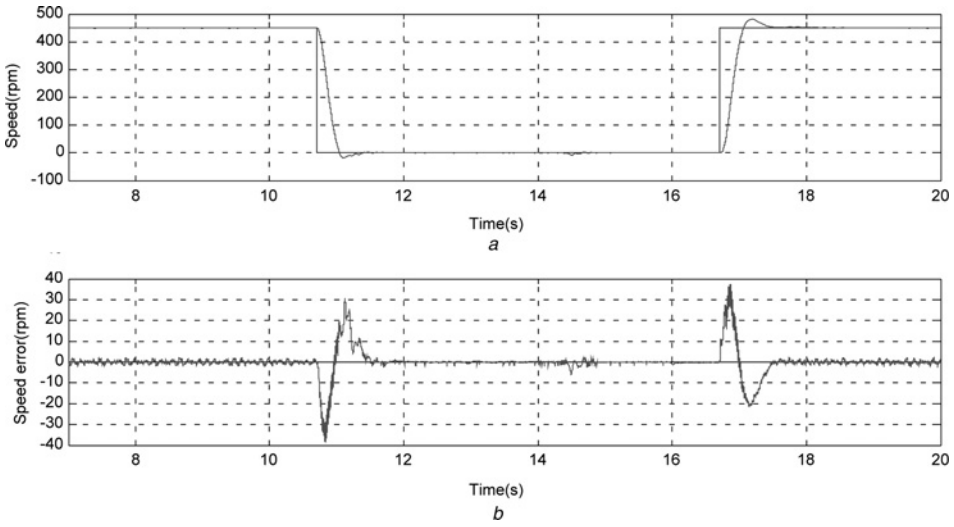

Fig. 10 *Fully sensorless speed control at no load using the proposed method*

a Reference speed and measured speed
b Speed error between measured speed and estimated speed

Figs. 10–12 show the results of full sensorless speed control under no load and loaded conditions using the proposed method. In Fig. 10 speed changes from 450 to 0 and back to 450 rpm are shown. The estimated speed and position seen in the figure proved that the system responded to step speed demands with good dynamic response and good steady-state behaviour, even at relatively high speeds. In Fig. 11 speed steps between 12 and −12 rpm were applied to the system at no load, and the speed and position response of the system measured using the encoder are shown for evaluation. The results show that the system works with a peak steady-state error below 7 rpm, and this is acceptable performance at low speed. Finally, Fig. 12 shows speed step changes between 30 and 0 rpm with 50% load applied to the system. Again the steady-state error measured using an encoder is below 5 rpm demonstrating excellent performance, and the transient response meets the design specification.

Fig. 13 shows the system response to a load steps between 0 and 50% load. The sensorless control is able to quickly respond to load changes and maintains good speed control.

To demonstrate the improvement in the current distortion obtained by applying the new scheme (multi-level INFORM method) compared to those obtained by applying the INFORM method and the FPE method on a two-level inverter, these methods were implemented on the experimental rig at two different loads and speeds. The stator current waveform was captured using an oscilloscope and current sensors [17, 18] and the THD was calculated offline. The excitation voltage used in the new scheme (multi-level INFORM method) was 150 V, whereas it is 620 V for the two-level INFORM method and the two-level FPE method.

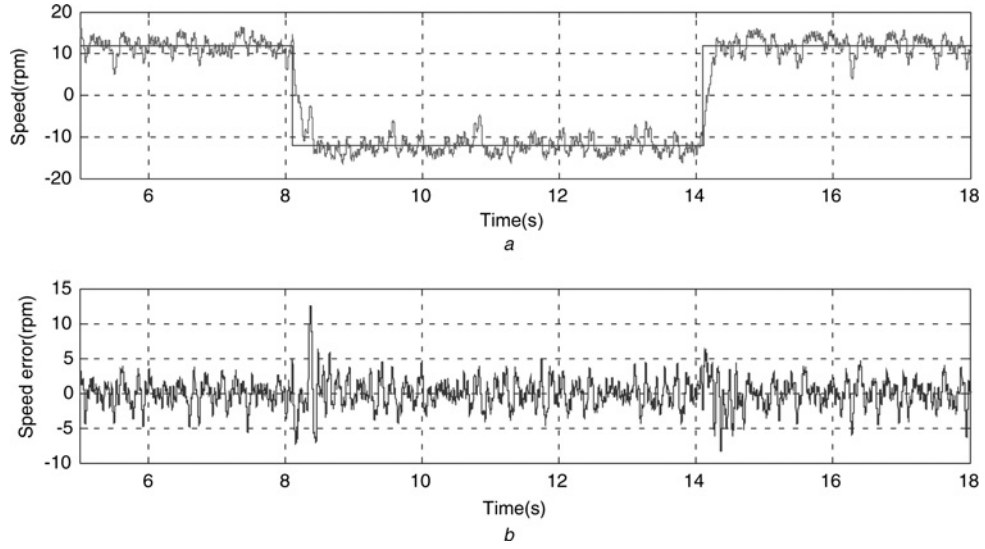

Fig. 11 *Fully sensorless speed control at no load using the proposed method*

a Reference speed and measured speed
b Speed error between measured speed and estimated speed

doi: 10.1049/iet-pel.2010.0264

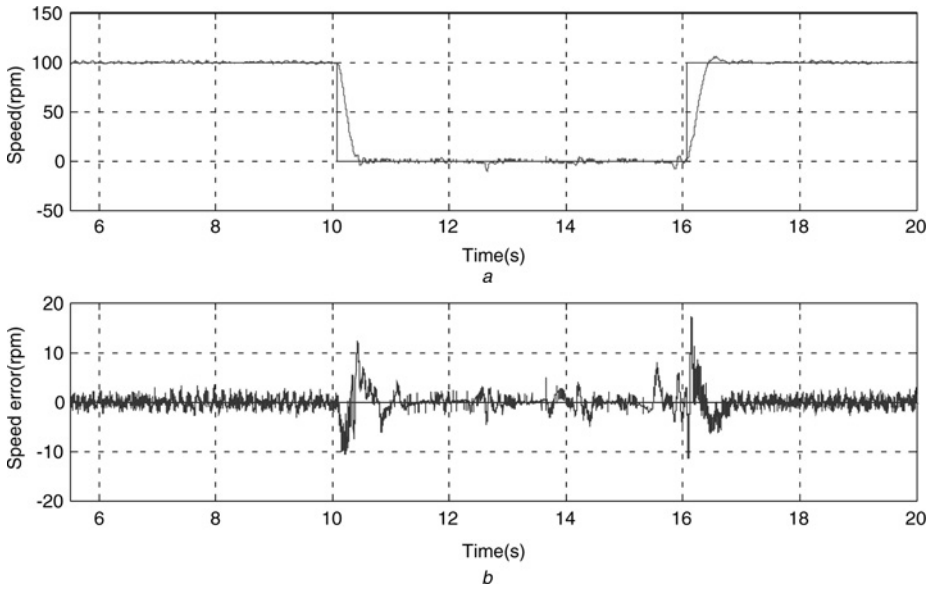

Fig. 12 *Fully sensorless speed control at 50% load using the proposed method*

a Measured speed and reference speed
b Speed error between measured speed and estimated speed

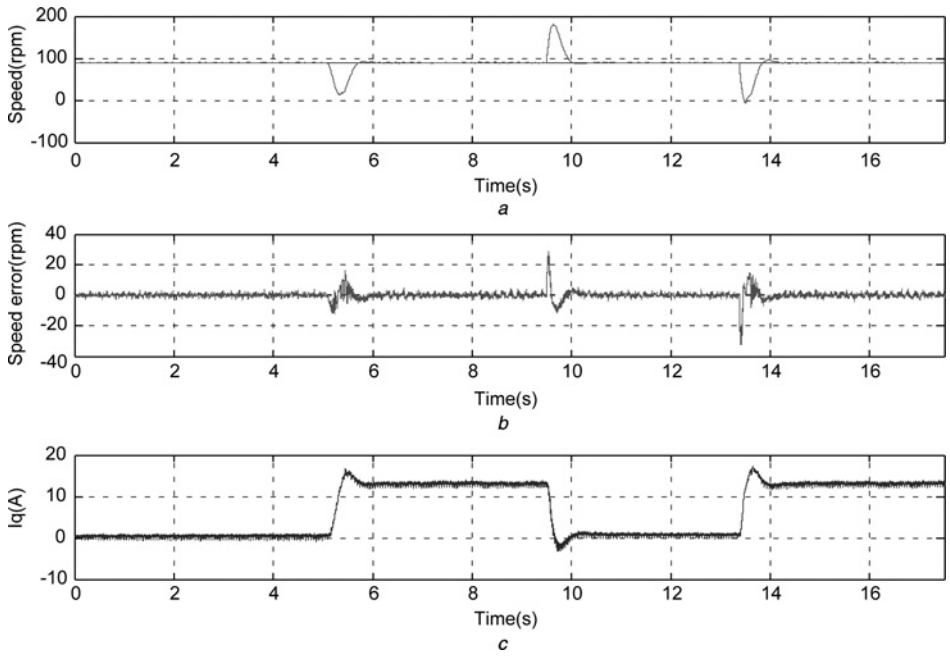

Fig. 13 *Load steps between 50% and 0 load using the multi-level inverter INFORM method*

a Measured speed reference speed
b Speed error between measured speed and estimated speed
c Iq

The 150 V excitation voltage helped to reduce the minimum pulse width (t_{min}) from 25 μs (used in the two-level methods) to 20 μs in the proposed multi-level method.

Fig. 14 shows the current waveforms measured while applying the different methods with the drive operating at 30 rpm at 35% load. The results shows that by using the new method (multi-level INFORM method), the THD was reduced from 6 and 4.5% for the two-level INFORM method and the two-level level PWM method, respectively, to 1.2% using the new method. Note that the THD of the motor current when operating in sensored mode is 1.04%. This improvement can also be noticed from the significant reduction in the audible noise level that is achieved when applying the new method.

When the drive is operated at 150 rpm and at no load, the measured THD of the motor current for the four different control methods is given in Table 1. The results in this test are similar to those of the previous test.

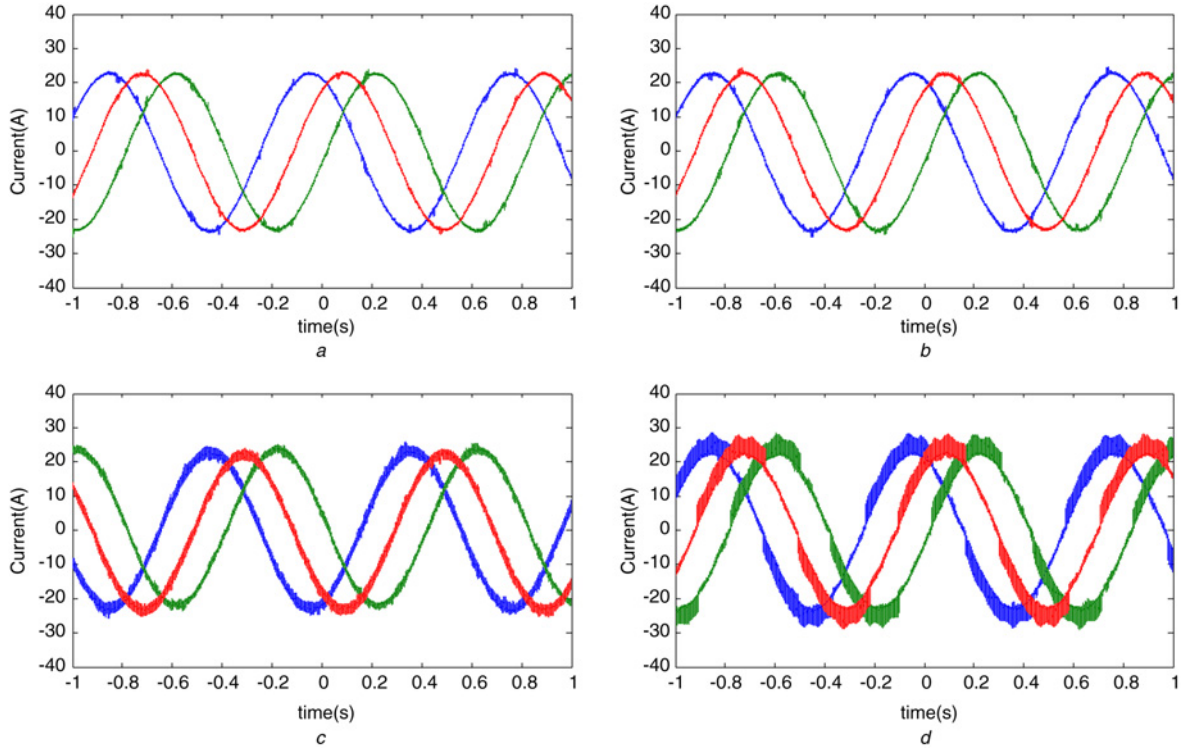

Fig. 14 *Current waveforms in different excitation methods at 30 rpm and 35% load*

a no excitation
b multi-level INFORM method
c two-level INFORM method
d two-level FPE method

Table 1 THD of line current for different excitation methods at 150 rpm and no load

	Two-level FPE method	Two-level INFORM	Two-level sensored control	Multi-level INFORM
THD	6.50%	5%	1.37%	1.60%

7 Conclusions

This paper has outlined a new scheme for rotor position estimation for an induction motor using low-voltage H-Bridges connected in series with a standard two-level inverter to generate test vectors. The specific aim was to demonstrate that if an approach such as the INFORM sensorless technique were to be implemented on a multi-level drive which uses different DC link voltages, then significant improvements could be made to the motor current waveform compared to if a similar sensorless drive were created using a two-level inverter. This has been demonstrated by comparing measurements of THD for the motor currents for each of these techniques implemented on a 16 kW experimental prototype. The performance of the sensorless control was shown to be excellent, both in steady state and during transient conditions.

The proposed multi-level INFORM method could be incorporated into multi-level drives which incorporate H-Bridges using only software modifications. These drives have been proposed for high-power applications [10], and are being considered for automotive applications [11]. The FPE method can also be incorporated into the multi-level drive to achieve further improvements to the motor current waveform, and a wider operating speed range. This will be the subject of future publications.

8 References

1 Jansen, P.L., Lorenz, R.D.: 'Transducerless position and velocity estimation in induction and salient AC machines', *IEEE Trans. Ind. Appl.*, 1995, **31**, pp. 240–247
2 Ha, J.-I., Ohto, M., Jang, J.-H., Sul, S.-K.: 'Design and selection of AC machines for saliency-based sensorless control'. Industrial Applications Conf. IEEE, IAS Annual Meeting, 2000, vol. 2, pp. 1155–1162
3 Linke, M., Kennel, R., Holtz, J.: 'Sensorless speed and position control of synchronous machines using alternating carrier injection'. IEEE Int. Electric Machines and Drives Conf. IEMDC03, 2003, vol. 2, pp. 1211–1217
4 Schroedl, M.: 'Sensorless control of AC machines at low speed and standstill based on the INFORM method'. IEEE IAS Annual Meeting, 1996, vol. 4, pp. 270–277
5 Holtz, J., Juliet, J.: 'Sensorless acquisition of the rotor position angle of induction motors with arbitrary stator windings'. IAS Annual Meeting, 2004, vol. 2, pp. 1675–1682
6 Qiang, G., Asher, G.M., Sumner, M., Makys, P.: 'Position estimation of AC machines at all frequencies using only space vector PWM based excitation'. Third IET Int. Conf., 2006, pp. 61–70
7 Robeischl, E., Schroedl, M.: 'Optimized INFORM measurement sequence for sensorless PM synchronous motor drives with respect to minimum current distortion', *IEEE Trans. Ind. Appl.*, 2004, **40**, pp. 591–598
8 Staines, C., Caruana, C., Asher, G.M., Sumner, M.: 'Sensorless control of induction machines at zero and low frequency using zero sequence currents', *IEEE Trans. Ind. Electron.*, 2006, **53**, pp. 195–206
9 Hua, Y., Sumner, M., Asher, G.M., Qiang, G.: 'Sensorless control for a PM machine with reduced current distortion using space vector PWM excitation'. EPE, Barcelona, 2009

doi: 10.1049/iet-pel.2010.0264

10 Manjrekar, M.D., Steimer, P.K., Lipo, T.A.: 'Hybrid multilevel power conversion system: a competitive solution for high-power applications', *IEEE Trans. Ind. Appl.*, 2000, **36**, pp. 834–841
11 Liu, H., Tolbert, L.M., Khomfoi, S., Ozpineci, B., Du, Z.: 'Hybrid cascaded multilevel inverter with PWM control method'. IEEE Power Electronics Specialist Conf., June 2008, pp. 162–166
12 Saleh, K., Asher, G.M., Sumner, M., Tomasini, M., Qiang, G.: 'Low speed sensorless control of an induction motor fed by multilevel converter to reduce current distortion'. EPE, Barcelona, 2009
13 Kempski, A., Smolenski, R., Kot, E.: 'Mitigation techniques of conducted EMI in multilevel inverter drives', *IEEE Compat. Power Electron.*, 2005, pp. 218–222
14 Makys, P., Asher, G.M., Sumner, M., Gao, Q., Vittek, J.: 'A low memory disturbance elimination method for sensorless control of induction motor drive using test vector injection'. IECON, 2006, pp. 1071–1076
15 Holtz, J., Pan, H.: 'Elimination of saturation effects in sensorless position controlled induction motors', *IEEE Trans. Ind. Appl.*, 2000, **40**, pp. 623–631
16 Lorenz, R.D., Van Patten, K.W.: 'High-resolution velocity estimation for all-digital, ac servo drives', *IEEE Trans. Ind. Appl.*, 1991, **27**, pp. 701–705
17 www.lecroy.com/tm/products/scopes/WaveRunner_6000A/WR6A_DC.pdf
18 www.lecroy.com/tm/products/probes/current/current_probes_datasheet.pdf